Available online at www.sciencedirect.com
SCIENCE DIRECT®
Journal of Power Sources 141 (2005) 326–339
JOURNAL OF POWER SOURCES
www.elsevier.com/locate/jpowsour

A simplified physics-based model for nickel hydrogen battery

Shengyi Liu[a,*], Roger A. Dougal[a], John W. Weidner[b], Lijun Gao[a]

[a] *Department of Electrical Engineering, University of South Carolina, Columbia, SC 29208, USA*
[b] *Department of Chemical Engineering, University of South Carolina, Columbia, SC 29208, USA*

Received 23 August 2004; accepted 30 September 2004
Available online 7 December 2004

Abstract

This paper presents a simplified model of a nickel hydrogen battery based on a first approximation. The battery is assumed uniform throughout. The reversible potential is considered primarily due to one-electron transfer redox reaction of nickel hydroxide and nickel oxyhydroxide. The non-ideality due to phase reactions is characterized by the two-parameter activity coefficients. The overcharge process is characterized by the oxygen reaction. The overpotentials are lumped to a tunable resistive drop to fit particular battery designs. The model is implemented in the Virtual Test Bed environment, and the characteristics of the battery are simulated and in good agreement with the experimental data within the normal operating regime. The model can be used for battery dynamic simulation and design in a satellite power system, an example of which is given.

Keywords: Nickel hydrogen battery; Non-ideal reversible potential; Overcharge; Self-discharge; Resistive-companion model

1. Introduction

Complicated electrochemical processes in a nickel hydrogen battery [1,2] involve more than eight reactions including main reactions, phase reactions, and side reactions. While a detailed model has been developed [3,4], it is currently coded in discipline-specific languages and for standalone simulation only. Thus, it is not in general available for use in system level simulation and design. This paper presents a simplified, yet still physics-based, model that can be rapidly implemented and conveniently used for the battery dynamic simulation, design, and optimization in complicated spacecraft power systems.

The model is based on following considerations. For typical applications (e.g., in spacecraft power systems [5–7]), the charge and discharge of the Ni–H_2 battery are in such a controlled way that the rate of charge and discharge is less than 0.5 C to ensure a reliable, safe and long lifetime operation [8,9]. Under such a circumstance, the charge, mass and heat transport, and the phase equilibrium can be assumed to complete instantly. Thus, the kinetics of reactions is less likely a limiting factor to the external characteristics. This leads to the assumption that the boundaries between the electrodes and the separator, and those between the gas phase and solid phase in the battery vanish, and the electrochemical and electrothermal processes take place uniformly throughout the battery. This assumption greatly simplifies the modeling process while observing the major features of the battery.

The present model is implemented in the Virtual Test Bed software environment [10], in which the battery is considered as an interdisciplinary (chemical, electrical and thermal) system governed by physics laws under certain initial and boundary conditions. Given a time, the battery interacts with surroundings in two ways: it delivers electrical power to the load at its electrical terminals during discharge by converting chemical energy into electric one (or the reverse during charge process), and it absorbs or releases heat to ambient at its external surface. Thus, the battery voltage is a result of coupled electrochemical, chemical-thermal and electrothermal processes.

* Corresponding author. Tel.: +1 803 777 8966; fax: +1 803 777 8045.
E-mail address: lius@engr.sc.edu (S. Liu).

0378-7753/$ – see front matter © 2004 Elsevier B.V. All rights reserved.
doi:10.1016/j.jpowsour.2004.09.035

Nomenclature

A	electrode area (m^2)
a	specific area ($m^2\ m^{-3}$)
$b_j(t-h)$	time history for the through variable at terminal j
C_b	battery capacity (A h)
c_p	average specific heat ($J\ kg^{-1}\ K^{-1}$)
E_{N_i}	total reversible potential (V)
E_{O_2}	oxygen reaction potential (V)
h	simulation time step (s)
F	Faraday constant (96,485 C mol^{-1})
$g_{j,k}$	admittance of a through variable at terminal j with respect to an across variable at terminal k
L_+	electrode thickness (m)
m	battery cell mass (kg)
i_{N_i}	nickel reaction current (A)
i_{O_2}	oxygen reaction current (A)
$i_{O_2,0}$	oxygen exchange current density ($A\ m^{-2}$)
i_T	thermal current ($W\ K^{-1}$)
n_{H_2}	amount of hydrogen (mol)
P	across variable for the pressure terminal (Pa)
p	pressure (Pa)
Q_{max}	maximum charge stored in the battery (C)
R	gas constant ($8.314\ J\ mol^{-1}\ K^{-1}$)
R_i	internal resistance (Ω)
T	battery bulk temperature, also across variable for thermal terminal (K)
t	independent variable time (s)
V_g	volume of battery (m^3)
v	battery terminal voltage (V)
v_a, v_c	across variables for anode and cathode (V)
x	state of discharge
α_{O_2}	oxygen reaction transfer number (0.75)

The solution to the coupled processes is obtained by means of the resistive-companion (RC) method [11], which requires the governing equations to be time-discretized to a standard matrix formulation in terms of across and through variables. The resulted matrix equations are then simultaneously solved through the VTB time-domain simulation using the nodal analysis approach.

2. Model description

2.1. Electrochemical process

The deviation of the reversible potential of the nickel electrode from the ideal Nernst equation, or its non-ideality, was interpreted [12] as due to intercalation of multi-phases, including α- and β-phase of nickel hydroxide, and β- and γ-phase of nickel oxyhydroxide. When discharging, it yields higher capacity [4] than that obtained from a single-phase nickel oxyhydroxide. As a first approximation, the overall potential can be characterized as if a usual one-electron transfer redox reaction occurs between nickel hydroxide and oxyhydroxide, but with the incorporation of the effects of both non-ideality due to multi-species of active nickel materials and the potential due to hydrogen reaction at the platinum electrode.

To characterize the overcharge process, the oxygen reduction is considered. It was believed [4] that the water oxidation/reduction (or oxygen evolution) at the nickel electrode and the oxygen reduction at the platinum electrode plays a dominant role in an overcharge process, causing a large portion of the current wasted. For normal charge and discharge, the oxygen reduction yields a negligible current.

Based on the above descriptions, the electrochemical reactions that characterize the energy conversion between chemical and electrical forms in the Ni–H_2 battery are given below.

At the nickel electrode are the nickel reduction/oxidation and the water reduction/oxidation:

$$\mathrm{NiOOH + H_2O + e^- \underset{\text{discharge}}{\overset{\text{charge}}{\rightleftarrows}} Ni(OH)_2 + OH^-}, \tag{1}$$

$$\frac{1}{2}\mathrm{O_2 + H_2O + 2e^- \rightleftarrows 2OH^-}. \tag{2}$$

At the platinum electrode are the hydrogen reaction and the oxygen reduction:

$$\frac{1}{2}\mathrm{H_2 + OH^- \underset{\text{discharge}}{\overset{\text{charge}}{\rightleftarrows}} H_2O + e^-}, \tag{3}$$

$$\tfrac{1}{2}\mathrm{O_2 + H_2O + 2e^- \rightarrow 2OH^-}. \tag{4}$$

The overall reversible potential can be described as:

$$E_{N_i}(T,x) = E^0_{N_i}(T) + \frac{RT}{F}\ln\left(\frac{1-x}{x}\right) + \frac{RT}{2F}[A_0(T)C(x) + B_0(T)D(x)]. \tag{5}$$

The third and the last term in (5) are the characteristics of the non-ideality, and,

$$A_0(T) = a_0 + a_1 T, \tag{6}$$

$$B_0(T) = b_0 + b_1 T, \tag{7}$$

$$C(x) = c_0 + c_1 x, \tag{8}$$

$$D(x) = d_0 + d_1 x + d_2 x^2, \tag{9}$$

$$E^0_{N_i}(T) = \begin{cases} e_{0d} + e_1 T, & \text{for discharge} \\ e_{0c} + e_1 T, & \text{for charge} \end{cases}, \tag{10}$$

where a_i, b_i, c_i, and d_i are constants for phase activities of nickel species, which may vary from one battery to another due to different contents and pore structures. e_{0c}, e_{0d} and e_1 are also constants. The difference between e_{0c} and e_{0d} in (10)

is used to characterize the hysteresis of proton intercalation in nickel hydroxide electrode [13,14].

Under the assumption of a uniform and non-kinetic limited reaction, the current from oxygen reaction can be calculated according to the Butler–Volmer equation,

$$i_{O_2}(v,T) = AL_+ ai_{0,O_2}(T) \times \exp\left[4(1-\alpha_{O_2})\frac{F}{RT}(v - E_{O_2}(T))\right], \quad (11)$$

where the exchange current density is of the Arrhenius type [3,4], and,

$$E_{O_2}(T) = 1.730 - 0.00168T, \quad (12)$$

$$ai_{O_2,0}(T) = 10.0 \exp\left[-12,025\left(\frac{1}{T} - \frac{1}{298}\right)\right]. \quad (13)$$

Eq. (12) is the simplified equilibrium potential of the oxygen reaction depending upon the temperature only. The numerical parameters appeared in (12) and (13) are calculated based on the data in references [3,4] that are specifically applied to the oxygen reaction in Ni–H_2 batteries.

The state of discharge x can be conveniently related to the nickel reaction current as:

$$\frac{dx}{dt} = -\frac{i_{N_i}}{Q_{max}}. \quad (14)$$

The battery terminal voltage can be related to the current:

$$v = E_{N_i} + R_i i_{N_i}. \quad (15)$$

The fitting parameter R_i accounts for the overall internal loss due to ohmic, surface kinetic and concentration limitations. Since the internal loss in the Ni–H_2 battery is generally small compared to most of other major secondary batteries, we simply use a small constant to approximate. Eqs. (4)–(15) complete the descriptions of the electrochemical process.

2.2. Thermal process

To simplify, we consider the heat generations due to the enthalpy of reactions [15] and the heat transported at the thermal terminal only, whereas the heat due to isometric process, enthalpy of mixing, phase change and change of specific heat are ignored without introducing significant error. The rate of temperature change of the battery is governed by the energy balance equation:

$$c_p m\frac{dT}{dt} = i_{N_i}\left(v - E_{N_i} + T\frac{\partial E_{N_i}}{\partial T}\right) + i_{O_2}\left(v - E_{O_2} + T\frac{\partial E_{O_2}}{\partial T}\right) + i_T T. \quad (16)$$

The first two terms on the right-hand-side are owing to the enthalpy of reactions, which can be identified as (1) polarization heat including $i_{N_i}(v - E_{N_i})$ and $i_{O_2}(v - E_{O_2})$, which are irreversible electrothermal processes; and (2) entropic heat including $i_{N_i}T(dE_{N_i}/dT)$ and $i_{O_2}T(dE_{O_2}/dT)$, which are reversible chemical-thermal processes. The last term on the right-hand side is the heat transported to (or from) the surroundings through the battery surface or the thermal terminal, which is expressed as the product of the through variable i_T (thermal current) and the across variable T (temperature).

2.3. Pressure modeling

The hydrogen pressure in the battery is an indicator for the state of discharge (hydrogen content) under the condition of regulated charge/discharge. Thus, a built-in sensor is used to detect the pressure [5], so that a *V*/*P* (voltage/pressure) control can be implemented to prevent the battery from overcharge. Assuming the ideal gas law applies, we then have:

$$p = \frac{n_{H_2}RT}{V_g}, \quad (17)$$

$$\frac{dn_{H_2}}{dt} = \frac{i_{N_i}}{2F}, \quad (18)$$

$$n_{H_2}|_{t=0} = \frac{3600C_b}{2F}(1 - x|_{t=0}) \quad (19)$$

The partial pressure of oxygen is ignored in this calculation. This is based upon the assumption that the reactions in the battery are uniform throughout, and the charge/discharge is not so fast that any appreciable oxygen produced will be immediately removed via reaction (4).

3. VTB implementation

The VTB implementation of the model described by Eqs. (5)–(19) involves (1) defining appropriate terminals for power or signal coupling; (2) deriving the terminal equations in their standard RC format for each terminal; and (3) developing C++ code for computer execution. The time-domain solution for coupled physics processes of the battery can then be obtained through VTB simulation for any given circuit configurations to which the battery is connected.

The physical electric terminals of the Ni–H_2 battery are its anode and cathode that can be connected to an external circuit for electrical power coupling. Naturally, the current for the through variable and the potential for the across variable are defined. The physical thermal terminal is the external surface through which the heat can transfer to or from the surroundings. By definition, the thermal terminal, or the battery surface can transport heat power by means of conduction, or radiation, or convection. The pressure terminal is a signal terminal. The signal from a built-in pressure sensor is coupled to an external circuit through this signal port for monitoring or control purposes. Thus, there is no actual

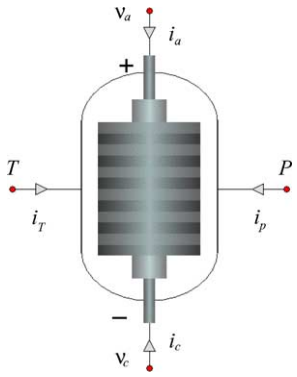

Fig. 1. VTB schematic view of the Ni–H_2 battery.

mass or energy flow at this terminal. This is the major difference between a signal terminal and a natural terminal, where the power is transported, such as the anode, cathode, and thermal terminal defined here. VTB implementation of the pressure signal terminal is to convert the pressure into a voltage signal while allowing an infinitesimal current at the terminal. This is shown in Appendix A.4. The definition of the terminals and terminal variables, together with the battery icon in the VTB schematic view, are shown in Fig. 1.

Observing that the electrochemical and electrothermal processes are coupled, the through variables are generally functions of all possible across variables. Specifically, we expect that,

$$i_j(t) = \sum_k g_{j,k}k(t) - b_j(t-h), \quad j,\ k = v_\mathrm{a},\ v_\mathrm{c},\ T,\ P, \tag{20}$$

where,

$$g_{j,k} = \left.\frac{\partial i_j}{\partial k}\right|_{t-h}, \text{ and } b_j(t-h) = -i_j(t-h) + \sum_k g_{j,k}k(t-h).$$

In above equations, j signifies for subscripts only, whereas k is used to denote both subscripts and across variables of v_a, v_c, T and P. In matrix notation, Eq. (20) is of the following form:

$$\boldsymbol{I}(t) = \boldsymbol{G}(t-h)\boldsymbol{V}(t) + \boldsymbol{B}(t-h), \tag{21}$$

where $\boldsymbol{I}(t) = \{i_k(t)\}_{4\times1}$, $\boldsymbol{V}(t) = \{k(t)\}_{4\times1}$, $\boldsymbol{G}(t-h) = \{g_{j,k}\}_{4\times4}$, and $\boldsymbol{B}(t-h) = \{b_j(t-h)\}_{4\times1}$, $j,\ k = v_\mathrm{a},\ v_\mathrm{c},\ T,\ P$.

The result for the RC equations of the electrical terminals (anode and cathode), thermal terminal and pressure signal terminal, based on the mathematical Eqs. (5)–(19), are summarized in Eq. (22) (the detailed derivation is provided in Appendix).

$$\begin{pmatrix} i_\mathrm{a}(t) \\ i_\mathrm{c}(t) \\ i_\mathrm{T}(t) \\ i_\mathrm{P}(t) \end{pmatrix} = \begin{pmatrix} g_{\mathrm{a,a}} & g_{\mathrm{a,c}} & g_{\mathrm{a,T}} & 0 \\ g_{\mathrm{c,a}} & g_{\mathrm{c,c}} & g_{\mathrm{c,T}} & 0 \\ g_{\mathrm{T,a}} & g_{\mathrm{T,c}} & g_{\mathrm{T,T}} & 0 \\ g_{\mathrm{P,a}} & g_{\mathrm{P,c}} & g_{\mathrm{P,T}} & g_{\mathrm{P,P}} \end{pmatrix} \begin{pmatrix} v_\mathrm{a}(t) \\ v_\mathrm{c}(t) \\ T(t) \\ P(t) \end{pmatrix} - \begin{pmatrix} b_\mathrm{a}(t-h) \\ b_\mathrm{c}(t-h) \\ b_\mathrm{T}(t-h) \\ b_\mathrm{P}(t-h) \end{pmatrix}. \tag{22}$$

The four-terminal RC model for the Ni–H_2 battery given by (22) is coded in C++ language, and then compiled into a model object. Within the VTB, the battery model, appeared as that in Fig. 1, can be easily inserted into any circuit for simulation. For the vector Eq. (22) to accurately represent the characteristics of the battery, the calculation of admittance matrix $\boldsymbol{G}(t-h)$ and the time history vector $\boldsymbol{B}(t-h)$ is critical. During simulation, the VTB solver seeks a solution to the nodal variables for the entire system for each time step. The results as functions of time can be displayed on the oscilloscope-like screens, or can be saved as data files for later use. Eq. (22) can yield satisfactory results provided that the simulation time step is sufficiently small.

4. Battery characteristics

4.1. Parameter setup

We first demonstrate the Ni–H_2 battery static characteristics using the circuit shown in Fig. 2, where the battery model is subject to a charge–overcharge–self-discharge–discharge test. The electrodes are connected to a current load that is capable of sourcing or sinking current. A heat sink with a large heat transfer coefficient is connected to the thermal terminal to maintain the battery temperature in nearly a constant. The heat sink may transport heat from the battery to the ambient, or vice versa. The pressure signal terminal is left open at the moment. The model represents a single battery cell consisting of a stack of 24 modules connected in parallel

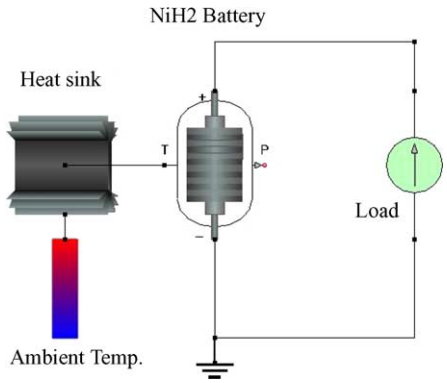

Fig. 2. VTB simulation circuit for the Ni–H_2 battery characteristics.

Table 1
Parameter setup for a single Ni–H_2 battery cell [4]

	Parameter	Value	Unit
Cell	Capacity	30	A h
	Volume	4.65×10^{-4}	m^3
	Mass	1.2	kg
	Resistance	0.01	Ω
	Surface area	0.06	m^2
	Specific heat	1000.0	$J\,kg^{-1}\,K^{-1}$
	No. of modules in series	24	
Module	Electrode area	0.005	m^2
	Electrode thickness	3.6×10^{-4}	m

Table 2
Parameters for multi-phase activity

$A_0(T)$	$a_0 = 11.50$, $a_1 = -0.0231$
$B_0(T)$	$b_0 = 32.00$, $b_1 = 0.060$
$C(x)$	$c_0 = 4.590$, $c_1 = 15.80$
$D(x)$	$d_0 = 1.800$, $d_1 = -5.680$, $d_2 = 0.350$
$E^0_{Ni}(T)$	$e_{0c} = 1.609$, $e_{0d} = 1.470$, $e_1 = 0.00062$

and contained in a cylindrical pressure vessel. Each module, characterized by Eq. (22), has a nickel electrode, platinum electrode, Zircar separator and polypropylene gas screen (for detailed constructions, please see references [2,4,8,9]). Other physical parameters are listed in Table 1. The parameters for multi-phase activity are given in Table 2. In the simulation, the initial temperature is set to the ambient temperature, and the initial state of discharge is set to 100%.

4.2. Temperature-dependent characteristics

The simulation was first conducted for a cycle of 16 h charge at a C/10 rate (3 A), 1 h self-discharge, and then a discharge at a C/2 rate (15 A) till it is depleted. The total runtime is 19 h. Shown in Fig. 3 is the load current profile.

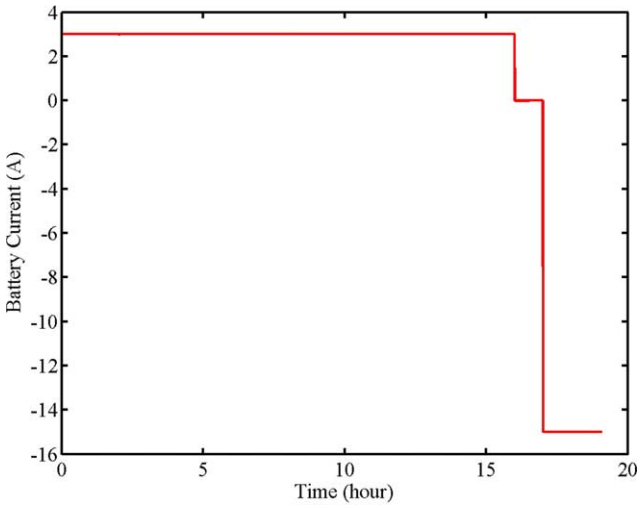

Fig. 3. The load current profile.

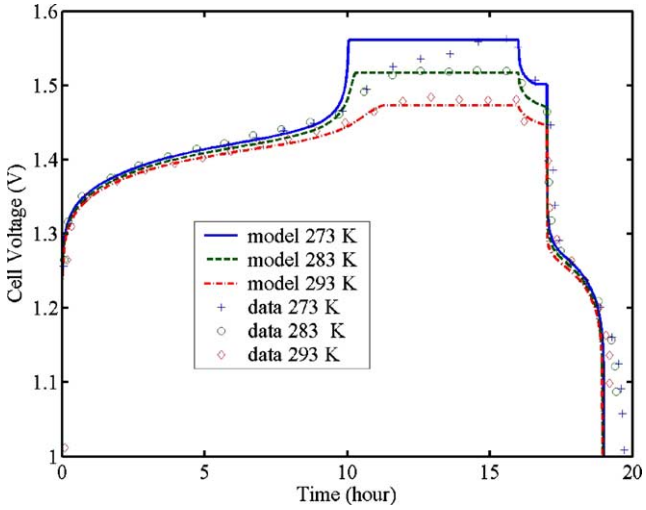

Fig. 4. Cell voltages for a cycle.

The cycle was repeated for three ambient temperatures −273, 283 and 293 K.

The battery cell voltage profiles (lines) are shown in Fig. 4 and compared against the TRW 30 A h cell data (points) [4]. As can be seen, the model fits the experimental data quite well for the normal charging (first 10 h) at all three temperatures. The model is also in good agreement with the data for self-discharge and discharge above 1.15 V (16–19 h). During overcharges, the model yields constant voltages, while the experimental data show slow ramps. This is primarily due to the temperature-dependent activities of the multi-species of nickel materials and possibly the non-linear overpotentials, which are not well characterized by the model. However, the ultimate overcharge voltages from the model are matched to those from the experiments. In addition, the simulated voltage behaviors are consistent with the data over the entire cycle. That is, lower temperatures yield higher voltages and also longer discharge life, suggesting that the battery is preferably operated at low temperatures. The discrepancy between the model and the data is also seen when discharging below 1.15 V, where the experimental data show larger discharge capacities. This is due to the appearance of γ-phase of nickel oxyhydroxide [4], which will be discussed further later. Nonetheless, it can be concluded that the model matches the experimental data very well within the normal operation range.

Figs. 5 and 6 show the currents from the nickel reaction and the oxygen reaction respectively for the same cycles. At any moment, the sum of the nickel current and the oxygen current is equal to the total current. These figures clearly show how a dominant nickel reaction in normal charge process transits to a dominant oxygen reaction in an overcharge process. During overcharges, the majority of a charge current is wasted for the oxygen reaction since the energy is not used for oxidizing nickel hydroxide. During a self-discharge process, the source of the oxygen current is the reduction of the nickel oxyhydroxide, thus yielding nickel and oxygen cur-

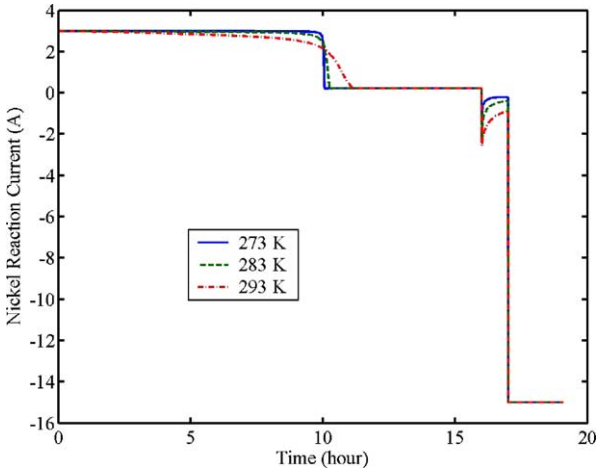

Fig. 5. The nickel reaction currents for a cycle.

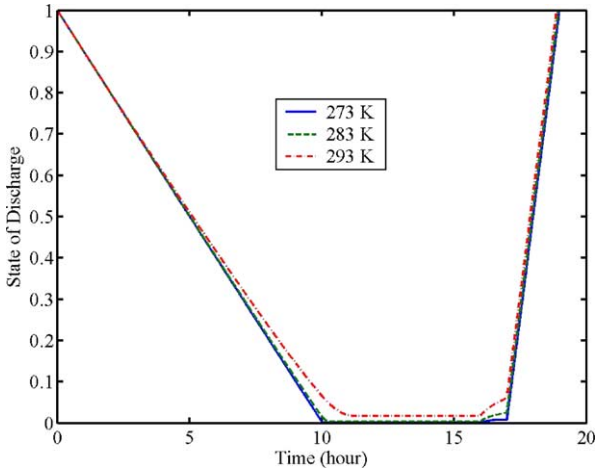

Fig. 7. The state of discharge for a cycle.

rents of equal amount but opposite directions. For a normal discharge, the oxygen current is usually minimal although it can be significant at high temperatures (see curves for 293 K).

The state of discharge, shown in Fig. 7, varies almost linearly for a constant charge or discharge rate. During an overcharge, the state of discharge maintains nearly a constant value. The value is higher for a higher temperature because more current goes to the oxygen reaction. Consequently, a lower overvoltage plateau results (see Fig. 4). The pressure profiles shown in Fig. 8 are complementarily similar to the states of discharge. This is in fact due to the stored hydrogen representing the charge state. However, since the pressure is not only proportional to the amount of hydrogen, but also to the temperature, it does not accurately represent the state of discharge. For example, the pressures are higher for higher temperatures for almost the entire cycle rather than lower to be consistent with the charge state behaviors, except at the joining area of normal charge and overcharge where a significant current loss to the oxygen reaction causes the pressure for 293 K to be lower than the pressure for 283 K. However, this does not generally affect the use of the pressure detection for overcharge protection. Thus, our simplified pressure modeling can still serve the purpose.

The temperatures of the battery for the cycle test are recorded in Fig. 9. Notice that the TRW 30 A h cell has an effective heat transfer area of 0.06 m^2. For maintaining a constant battery temperature during the test, the cooling coefficient can be as large as 60 $W\,m^{-2}\,K^{-1}$ [4], which is reasonable for a forced convection cooling. In our simulation, the rate of heat transfer was set equivalently to 3.6 $W\,K^{-1}$, so the conditions for cooling are comparable to the experimental condition. Fig. 9 shows the battery cell temperatures are slightly higher than the ambient during charging for each test, but with small variations. During discharge, the temperature increases significantly due to two reasons: (1) the overpotential heat due to a large discharge current, and (2) the reversible heat release during electrochemical reactions. Clearly the heat generation rate exceeds the surface transfer rate and therefore causing the temperature

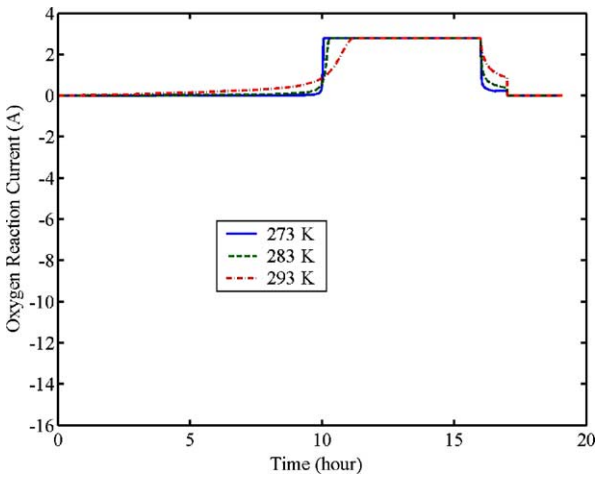

Fig. 6. The oxygen reaction currents for a cycle.

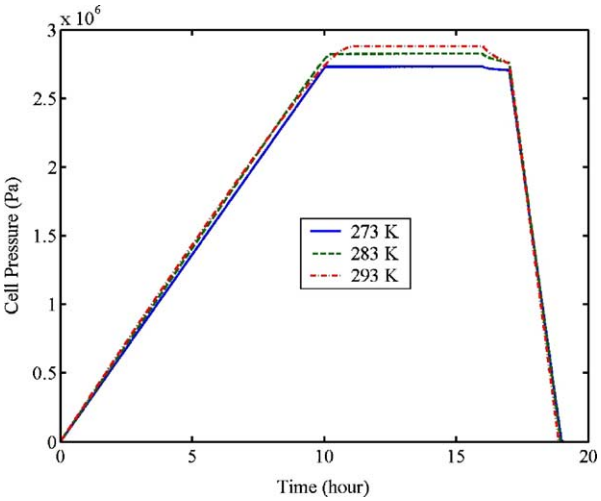

Fig. 8. The battery pressures for a cycle.

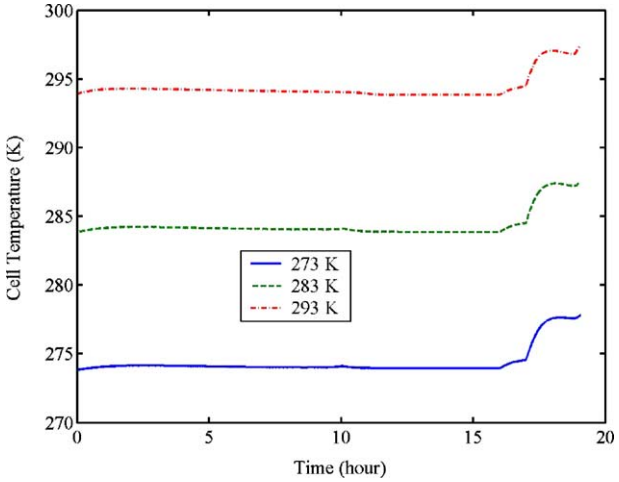

Fig. 9. The battery cell temperature variations for a cycle.

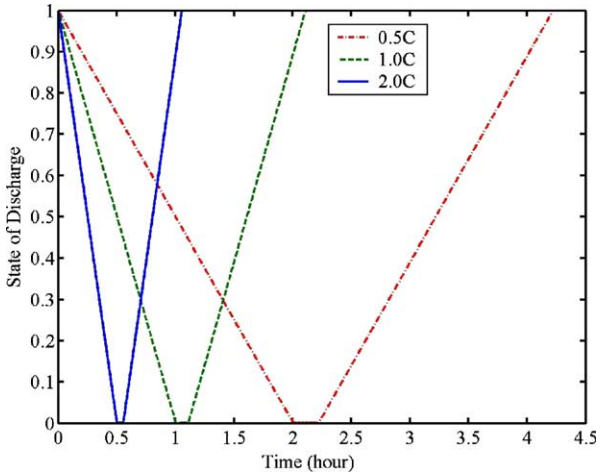

Fig. 11. The state of discharge for different rates.

to rise. Because of a large cooling coefficient and a small cell mass, a thermal equilibrium between the battery and the ambient was quickly reached. This is shown by the fact that the cell temperature reaches a constant value soon after the battery transits from one steady-state mode to another.

4.3. Rate-dependent characteristics

Figs. 10–13 show the battery characteristics under three charge/discharge rates: 0.5, 1.0 and 2.0 C. The ambient temperature is 283 K. For the three rates, the battery was charged for 2.2, 1.1 and 0.55 h respectively, and then discharged for 2, 1 and 0.5 h, respectively. In Fig. 10, both the voltages (thick lines) and the reversible potentials (thin lines) are shown. For discharging at high rates, the battery voltages are considerably lower than its reversible potentials due to significant internal loss that is typical to all batteries. For overcharge, the holding potentials are higher for higher rates due to a lower temperature (reversible heat effect). Figs. 11 and 12

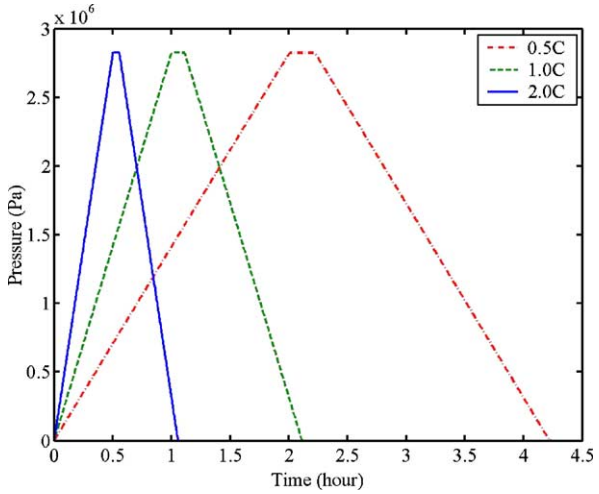

Fig. 12. The cell pressures for different rates.

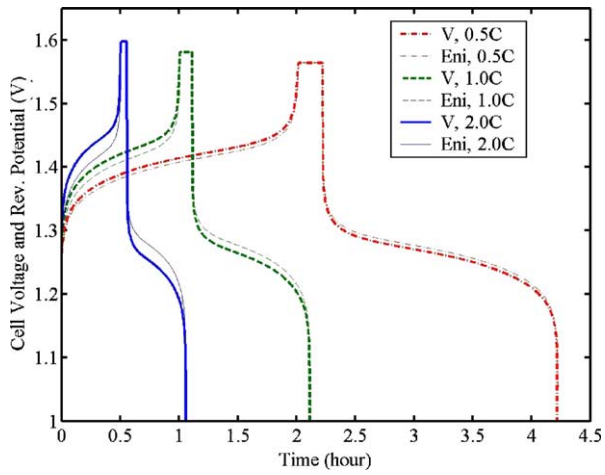

Fig. 10. The cell voltages (thick lines) and the reversible potentials (thin lines).

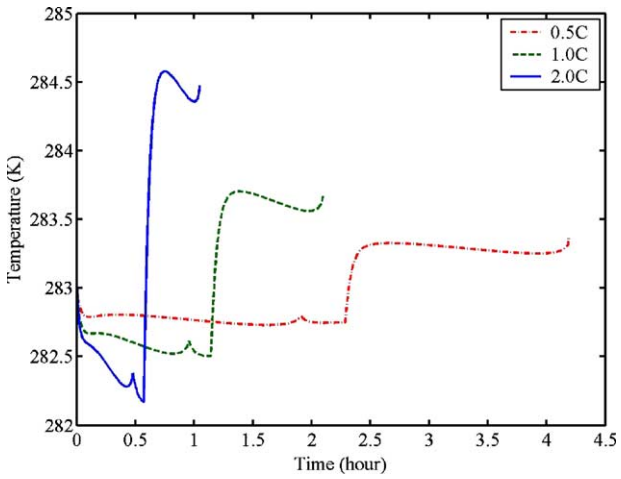

Fig. 13. The battery temperatures for different rates.

are the correspondent states of discharge and pressures for the three rates, showing similar characteristics to those in previous simulations.

Fig. 13 shows the cell temperature for the three rates. It is lower than the ambient during charging processes, higher than the ambient in discharging processes. Apparently, the reversal of the entropic heat in charging process causes the temperature to drop. During discharging, the release of entropic heat and irreversible heat result in higher temperatures. It is worth to remark that the temperature drop during charging was also noticed in reference [4]. Our next work is to improve the thermal modeling once the data are available for characterization.

5. Battery dynamics in a system

5.1. System description

The dynamic behavior of the Ni–H_2 battery in a simplified spacecraft electric power system, established in VTB as shown in Fig. 14, is simulated. The spacecraft is a low-earth-orbit (LEO) satellite having an average altitude of 798 km, an inclination angle of 60°, and an orbit of about 100 min, of which 35 min are the shadow time.

The energy source for the system is a solar array (SA). The Ni–H_2 battery array stores energy at the sun-view time, and provides power to the load at the earth-shadow time. In order for the battery to operate properly, a constant-current/constant-voltage/pressure-limited algorithm is employed for charge control and protection. The algorithm is implemented using the following components: a step-down (buck) converter, a PID controller, sensors, and diodes. The details of these component models can be found in VTB website [16], will not be described here. The signals of the battery voltage and current are sent to the controller for appropriate execution of the algorithm. In addition, the pressure signal feeds the controller for overcharge protection. Heat sinks to both the solar array and the battery transport the heat to ambient. For simplicity, a single load – transmitter – is used in the system.

Table 3
Parameter setup for the spacecraft power system

Parameter	Specification
Spacecraft orbit	Altitude 798 km, inclination 60°, orbit period 100 min
Solar array	100S × 30P cells. Cell V_{oc} = 0.615 V, area 0.01 m^2, series resistance 10 mΩ
Battery array	24S × 8P cells. The cell parameters are given in Table 1
Controller	Constant-current 32 A, constant-voltage 36 V, pressure limit 2.6 × 10^6 Pa
Transmitter	3.25 kW active, 0.25 kW sleeping. Duty ratio 50%, period 17.5 min

The system configuration is not necessarily optimized. However, the solar array size is chosen such that, without shunt regulation, it delivers a power to the load and the battery at a high efficiency (11.5% at a high power phase). The battery is sized by considering (1) it stores and delivers a nearly equal amount of energy in each orbit without experiencing a deep discharge hazard; (2) the capacity of the battery is designed to meet the end of life (EOL) requirement based on the Space Systems Loral performance-based battery design life model [8,9]. That is, with a temperature of 283 K and a maximum depth of discharge of 35%, the model yields a battery life of about 6.5 years. The parameter setup for the major components of the system is listed in Table 3. These numbers are chosen to meet the above criteria for demonstration and observation of the battery dynamic behaviors in a simplified system environment.

5.2. Simulation results

The total simulation time is 233.3 min, about 2.33 orbits. The results are shown by Figs. 15–23. Fig. 15 shows the orbit solar insolation received by the solar array while it is orbiting. The insolation level is 1357 W m^{-2} when the array sees the sun, and it drops to zero at the shadow period. The load power drawn by the transmitter is shown in Fig. 16. Notice that the transmitter was operated at the specified power levels and cycle rate regardless of the insolation levels at the solar array. Obviously, at the shadow

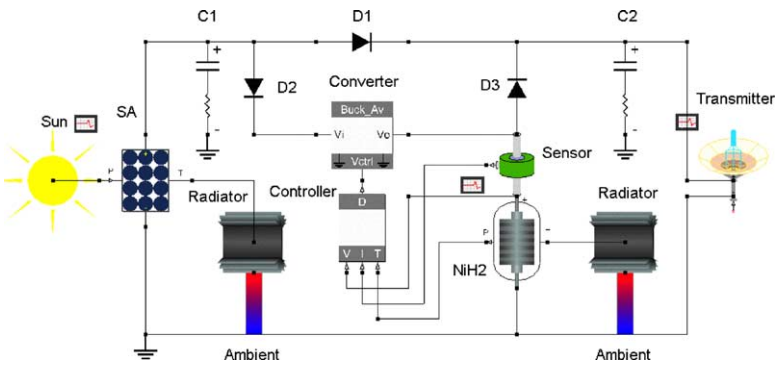

Fig. 14. Spacecraft power system using Ni–H_2 battery as an energy storage device.

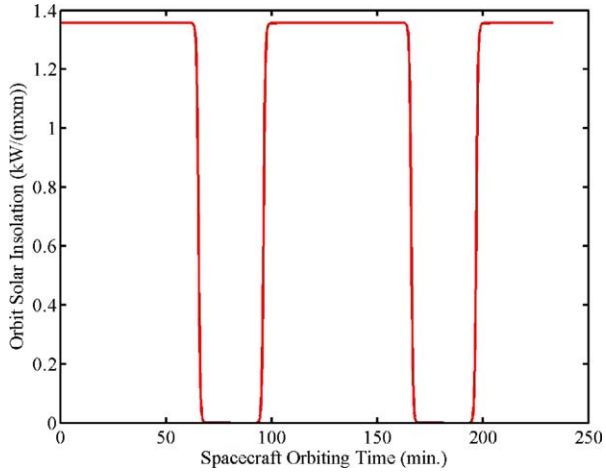

Fig. 15. Insolation received by the solar array as a function of orbiting time.

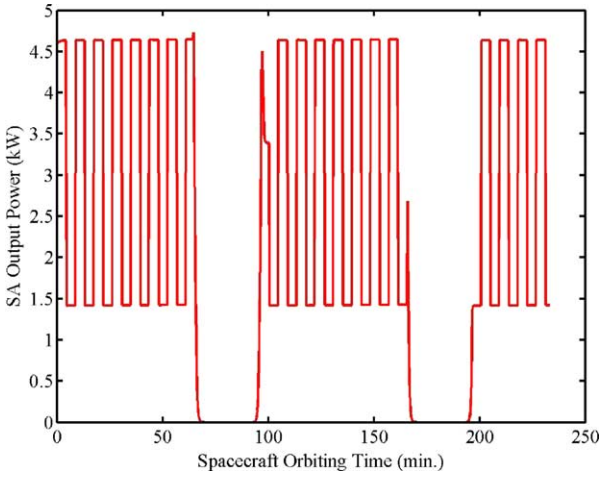

Fig. 17. The solar array output power for 2.33 orbits.

time, the transmitter power was provided by the battery array.

Fig. 17 shows the solar array power. At the sun-view time, the solar array converts the solar energy and sends power to the load as well as to the battery. Due to a pulsed load, the output power is also pulsating. For a high-power load of 3.25 kW, the solar array power is 4.64 kW with an efficiency of 11.5% and a voltage of 59.5 V. For a low-power load of 0.25 kW, the array power is about 1.42 kW with an efficiency of 3.5% and a voltage of 55.4 V. At the earth-shadow time, the solar array power is zero, leaving the battery to supply the power to the load. The details of the solar array characteristics, including voltage, current, efficiency and temperature, are available from the simulation, but will not be covered here since it is not a focus of this paper.

The battery behaviors in orbit are shown in Figs. 18–23. At the sun-view time, the battery is charging, having an increasing voltage from 34.3 to 34.7 V (Fig. 18) and a constant current of 32 A (Fig. 19), a rate of C/7.5. The positive power (about 1.1 kW, Fig. 20) indicates that the battery is absorb-

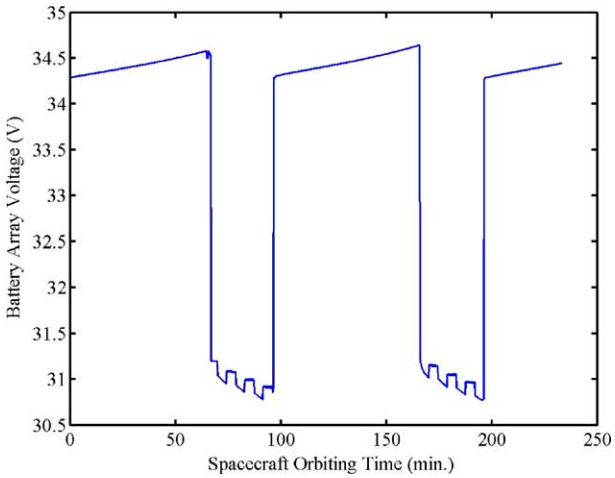

Fig. 18. The battery array voltage for about 2.33 orbits.

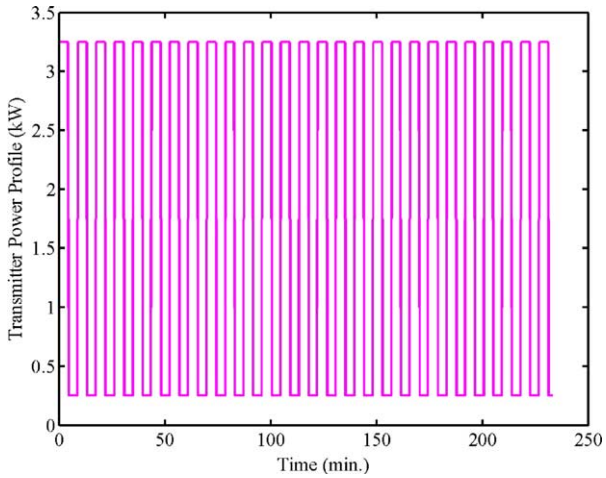

Fig. 16. The transmitter power profile as a function of time.

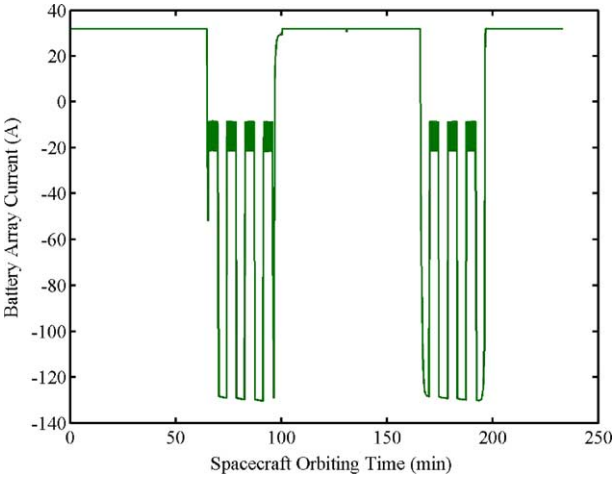

Fig. 19. The battery array current for about 2.33 orbits.

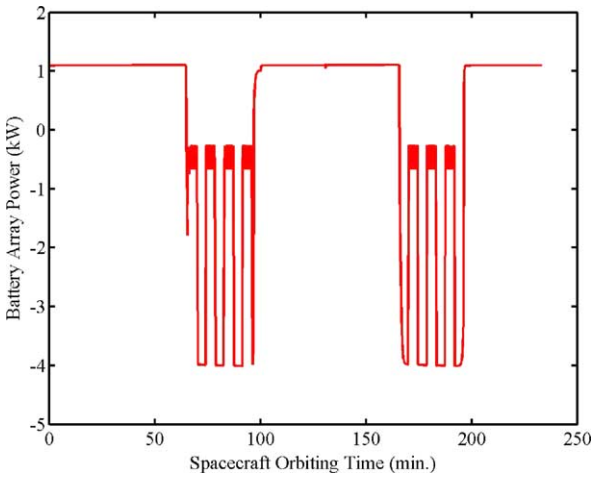

Fig. 20. The battery array power for about 2.33 orbits.

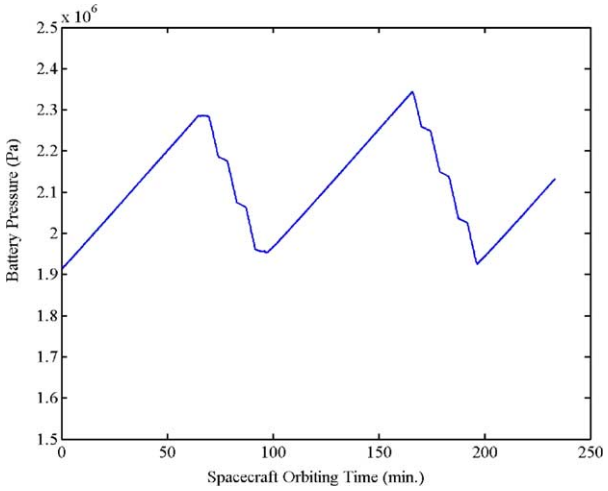

Fig. 22. The battery pressure for about 2.33 orbits.

ing power. The power relations among the source power in Fig. 17, the load power in Fig. 16, and the stored power in Fig. 20 reveal that there is a power loss about 0.29 kW at a high-power load, and a loss of 0.07 kW at a low-power load, which are caused by the resistances of circuit components.

At the earth-shadow time, the battery takes the duty to deliver power to the load at a voltage around 31 V. The current has large ripples due to a pulsed power load. For a high-power load of 3.25 kW, the battery discharge current is 130 A, equivalent to a rate of approximately C/2; while for a low-power load of 0.25 kW, the averaged discharge current is 12.8 A, a rate of about C/19. The battery output power (negative) is 4 kW for a high-power phase and averaged 0.4 kW for a low-power phase. The system losses are 0.75 kW for high-power phase, and 0.15 kW for a low-power phase. These losses are primarily due to large battery currents while operating at a low bus voltage, as the system is not an optimized design.

Figs. 21 and 22 show the state of discharge and the pressure respectively, which restore their initial values at the end of each orbit, since the total energy stored and the delivered in one orbit are nearly balanced. The state of discharge at the end of an orbit is about 0.3, equivalent to a depth of discharge 70%, well above the depth of discharge 35% requirement for 6.5 years life according to the Space Systems Loral performance-based battery life model [8,9].

The battery temperature variation during the course of orbiting is shown in Fig. 23. The thermal environment in the LEO is a result of solar insolation, earth albedo, earthshine, spacecraft heat generation, and space heat sink [17]. In this study, an equilibrium state for the thermal environment is assumed for simplicity, which possesses a temperature of 273 K. For the Ni–H_2 battery to have a better cycle life, it is important to control the battery not to operate in high temperature regimes. We have chosen the heat dissipater such that the temperature of the battery does not exceed 283 K during operation to satisfy 6.5 years life requirement. As shown in Fig. 23, the battery temperature has an about 10 K swing (270–280 K) for each orbit. The temperature decreases for

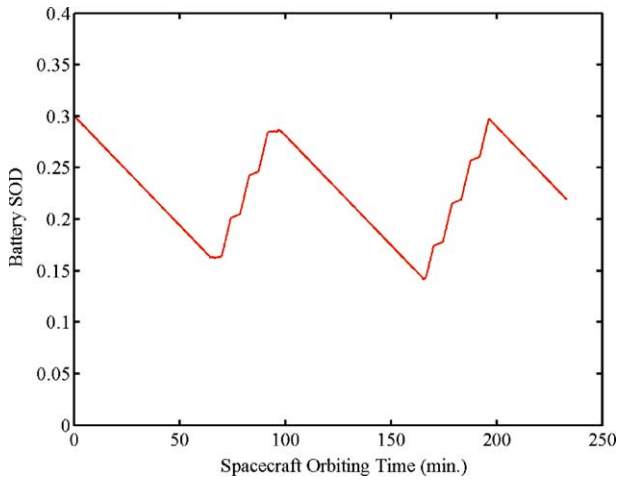

Fig. 21. The state of discharge of the battery for about 2.33 orbits.

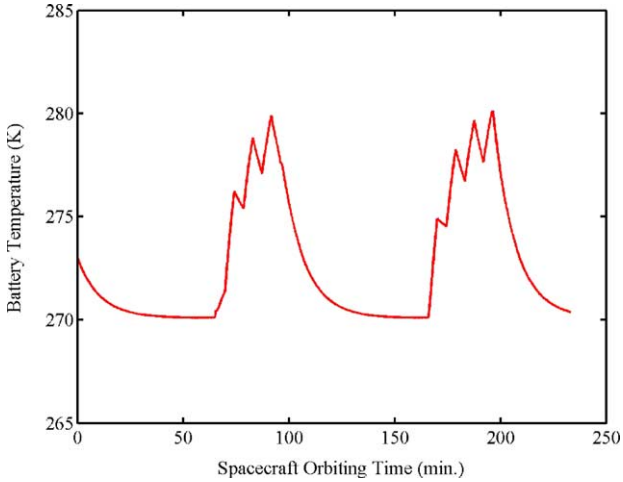

Fig. 23. The battery temperature for about 2.33 orbits.

a charging mode. This is again due to, in addition to the heat transfer, the electrochemical reactions that absorb the reversible heat. During a discharge mode, heat is released from the both reversible and irreversible processes, causing the temperature to rise. However, for a low discharge current, the rate of heat dissipation is higher than that of generation, yielding a temporary temperature drop. This is shown by the jagged temperature profile when the spacecraft is in the earth shadow time.

6. Discussion

The present model for the Ni–H_2 battery is based on a first approximation—uniform reactions, no rate and concentration limitations, and the two-parameter activity coefficient characterization of phase activities. The model allows to predict the battery behaviors and to perform preliminary system level design and analysis under the conditions of a regulated charge/discharge protocol. However, like any other models, the present model has several limitations.

The first noticeable limitation is that, as shown in Fig. 4, the model does not agree with the data for the discharge below 1.15 V. The discharge plateau appeared near 1.15 V is due to the activity of the γ-phase nickel oxyhydroxide, for which, apparently, the two-parameter activity coefficient method does not characterize very well. The charge stored in the γ-phase, according to [4], makes up about 30% of the total active material. The conversion to the γ-phase occurs mainly in an overcharge process at a cost of decreasing the β-phase oxyhydroxide. During discharge, two major parallel processes compete: one is the conversion from the β-phase oxyhydroxide to the hydroxide, the other is from the γ-phase oxyhydroxide to the hydroxide, and both are strongly temperature-dependent and contribute to the discharge capacity. On the other hand, charging at high temperatures does not yield a complete oxidation of the hydroxide, which conversely affects the discharge capacities. This is shown by the data in Fig. 4 that a larger discharge capacity results at a lower temperature, and the voltage discrepancy is decreased at high temperatures. Without an overcharge, the fraction of the γ-phase is less than 10%, whereas the β-phase is nearly 90%. Based on this analysis, we can conclude that the present model best applies to the case in which the battery is operated at a low temperature (between 273 and 283 K), and is controlled such that it does not undergo an overcharge process. Otherwise, the model incurs an error of 30%, for which the lower voltage limit (1.15 V) corresponds to an actual depth of discharge of about 30%. It is possible in the future to characterize the phase activities using three- or four-parameter activity coefficients for improving the model behaviors in overcharge and deep discharge regimes.

The thermal modeling mainly considers the constant overpotential loss and the reversible heat, which best applies to the case of a controlled charge/discharge scenario described in Section 5. The bulk temperature is usually lower than that of porous electrodes where most of heat is generated. Thus, the model is prone errors if overcharge, deep discharge, and high-rate discharge occur. The error may also result from following sources. (1) Several thermal effects are ignored in the model, such as heat due to isometric process, enthalpy of mixing, phase change and change of specific heat. (2) The non-linear feature of overpotential loss is not included. (3) The two-parameter activity coefficient method may also result in discrepancy in reversible heat. These features can be included and improved in the future modeling using detailed thermodynamic data, which, unfortunately, are not available at this time.

Finally, the model does not include capacity fade effect. However, the battery array can be sized based on the Space Systems Loral performance-based battery design life model [8,9] using the present model, as explained in Section 5. To ensure a safe, reliable and long lifetime, the spacecraft battery discharge rate is controlled not to exceed C/2.0, the discharge voltage not to exceed the lower limit of 1.15 V, and the temperature not to exceed 283 K. The system design can be improved if a practical load profile is given by utilizing an appropriate bus voltage level and a regulation method, and by optimizing solar array and battery array sizes. Though it is not optimized, the present system still allows performing preliminary studies of the dynamic behaviors of the Ni–H_2 battery in a LEO space environment.

7. Conclusion

The Ni–H_2 battery model based on the thermodynamics of one-electron redox reaction between nickel hydroxide and nickel oxyhydroxide is established in the VTB. The battery is assumed uniform throughout, and it is not subject to rate and concentration dependencies, which allows great simplification in mathematical treatment. The non-ideality of the reversible potential is characterized by the two-parameter activity coefficients. The overcharge and the self-discharge processes are characterized by the oxygen reaction. The details of the energy conversion processes are discussed and the VTB implementation of the model is presented. The model allows for the battery behaviors to be studied in a configurable system while it is dynamically interacting with the system and the environment. The simulation results show that the model in general has a good agreement with the experimental results above a voltage of 1.15 V, below which the discrepancy appears if the battery is overcharged prior to discharge. The future research will be devoted to improving the characterization of thermal behaviors, non-linear overpotentials, and the phase activities.

Acknowledgements

This work was sponsored jointly by Veridian M.R.J. under contract 00-MRJ-1085-100, by the US Army Com-

munications and Electronics Command and the National Reconnaissance Office under contract NRO-00-C-1034.

Appendix A

A.1. Useful expressions

Since the analytical expressions for the potentials of the nickel and oxygen reactions are given (Eq. (5) and (12)), they, together with their derivatives, can be accurately computed. Thus, we will seek expressions for the admittance matrix elements expressed in terms of potentials and their derivatives, which are given as:

$$\frac{\partial E_{N_i}}{\partial x} = -\frac{RT}{F}\left(\frac{1}{x(1-x)} - \frac{1}{2}[A_0(T)C'(x) + B_0(T)D'(x)]\right), \tag{A1}$$

$$\frac{\partial E_{N_i}}{\partial T} = e_1 + \frac{E_{N_i} - E^0_{N_i}}{T} + \frac{RT}{2F}[A'_0(T)C(x) + B'_0(T)D(x)], \tag{A2}$$

$$\frac{\partial^2 E_{N_i}}{\partial T^2} = \frac{R}{F}[A'_0(T)C(x) + B'_0(T)D(x)], \tag{A3}$$

$$\frac{\partial^2 E_{N_i}}{\partial x \partial T} = -\frac{R}{F}\left(\frac{1}{x(1-x)} - \frac{1}{2}[A_0(T)C'(x) + B_0(T)D'(x)] - \frac{T}{2}[A'_0(T)C'(x) + B'_0(T)D'(x)]\right), \tag{A4}$$

$$\frac{\mathrm{d}E_{O_2}}{\mathrm{d}T} = -0.00168. \tag{A5}$$

A.2. Electrical terminal

The terminal variables can be related to the battery current and voltage as

$$i_a(t) = -i_c(t) = i_{N_i}(t) + i_{O_2}(t), \tag{A6}$$

$$v_a(t) - v_c(t) = v(t) = E_{N_i}(t) + R_i i_{N_i}(t). \tag{A7}$$

Since the state of discharge is not a terminal variable, it is necessary for the device object to compute x during each time step. To do so, Eq. (14) is discretized in the time domain using Gear's 2 [18],

$$i_{N_i}(t) = -\frac{Q_{\max}}{2h}[3x(t) - 4x(t-h) + x(t-2h)]. \tag{A8}$$

Combining Eq. (A7) and (A8), we have.

$$\frac{v_a(t) - v_c(t) - E_{N_i}(t)}{R_{\mathrm{int}}} = -\frac{Q_{\max}}{2h}[3x(t) - 4x(t-h) + x(t-2h)]. \tag{A9}$$

Eq. (A9) can be solved for $x(t)$ numerically for given terminal across variables.

The nickel current component can be derived from Eqs. (5) and (A7). This is,

$$i_{N_i}(t) = \sum_k g_{N_i,k}k(t) - b_{N_i}(t-h), \quad k = v_a,\ v_c,\ T,\ P, \tag{A10}$$

where,

$$\begin{cases} g_{N_i,\mathrm{a}} = \dfrac{1}{R_{\mathrm{int}} + (\partial E_{N_i}/\partial x)/(\partial i_{N_i}/\partial x)|_{t-h}} \\ g_{N_i,\mathrm{c}} = -g_{N_i,\mathrm{a}} \\ g_{N_i,\mathrm{T}} = -\dfrac{1}{R_{\mathrm{int}}}\dfrac{\partial E_{N_i}}{\partial T}\Big|_{t-h} \\ g_{N_i,\mathrm{P}} = 0 \end{cases}, \tag{A11}$$

$$b_{N_i}(t-h) = -i_{N_i}(t-h) + \sum_k g_{N_i,k}k(t-h), \quad k = v_a,\ v_c,\ T,\ P. \tag{A12}$$

For the oxygen current component, since it is an explicit function of the terminal variables, it is straightforward to find the standard expression, as given below.

$$i_{O_2}(t) = \sum_k g_{O_2,k}k(t) - b_{O_2}(t-h), \quad k = v_a,\ v_c,\ T,\ P, \tag{A13}$$

where,

$$\begin{cases} g_{O_2,\mathrm{a}} = 4(1-\alpha_{O_2})\dfrac{F}{RT}i_{O_2}\Big|_{t-h} \\ g_{O_2,\mathrm{c}} = -g_{O_2,\mathrm{a}} \\ g_{O_2,\mathrm{T}} = \left(\dfrac{12,025}{T^2} - 4(1-\alpha_{O_2}) \times \dfrac{F}{RT^2}\left(v_a - v_c - E_{O_2} + T\dfrac{\mathrm{d}E_{O_2}}{\mathrm{d}T}\right)\right) i_{O_2}\Big|_{t-h} \\ g_{O_2,\mathrm{P}} = 0 \end{cases}, \tag{A14}$$

$$b_{O_2}(t-h) = -i_{O_2}(t-h) + \sum_k g_{O_2,k}k(t-h), \quad k = v_a,\ v_c,\ T,\ P. \tag{A15}$$

Using (A10) and (A13) in (A6), it can be found the equations for the anode and cathode are,

$$\begin{pmatrix} i_{\mathrm{a}}(t) \\ i_{\mathrm{c}}(t) \end{pmatrix} = \begin{pmatrix} g_{\mathrm{a,a}} & g_{\mathrm{a,c}} & g_{\mathrm{a,T}} & g_{\mathrm{a,P}} \\ g_{\mathrm{c,a}} & g_{\mathrm{c,c}} & g_{\mathrm{c,T}} & g_{\mathrm{c,P}} \end{pmatrix} \begin{pmatrix} v_{\mathrm{a}}(t) \\ v_{\mathrm{c}}(t) \\ T(t) \\ P(t) \end{pmatrix} - \begin{pmatrix} b_{\mathrm{a}}(t-h) \\ b_{\mathrm{c}}(t-h) \end{pmatrix}, \tag{A16}$$

where,

$$\begin{cases} g_{\mathrm{a,a}} = -g_{\mathrm{c,c}} = g_{N_i,\mathrm{a}} + g_{\mathrm{O_2,a}} \\ g_{\mathrm{a,c}} = -g_{\mathrm{c,c}} = g_{N_i,\mathrm{c}} + g_{\mathrm{O_2,c}} \\ g_{\mathrm{a,T}} = -g_{\mathrm{c,T}} = g_{N_i,\mathrm{T}} + g_{\mathrm{O_2,T}} \\ g_{\mathrm{a,P}} = -g_{\mathrm{c,P}} = 0 \end{cases}, \tag{A17}$$

$$b_{\mathrm{a}}(t-h) = -b_{\mathrm{c}}(t-h) = b_{N_i}(t-h) + b_{\mathrm{O_2}}(t-h). \tag{A18}$$

A.3. Thermal terminal

Construction of the thermal terminal is based on Eq. (16), which can be rearranged, after time-discretizing, as:

$$\begin{aligned} i_{\mathrm{T}}(t) = {} & \frac{c_p m}{2hT(t)}[3T(t) - 4T(t-h) + T(t-2h)] \\ & - \frac{i_{N_i}(t)}{T(t)}\left[v_{\mathrm{a}}(t) - v_{\mathrm{c}}(t) - E_{N_i}(t) + T(t)\frac{\partial E_{N_i}}{\partial T}(t)\right] \\ & - \frac{i_{\mathrm{O_2}}(t)}{T(t)}\left[v_{\mathrm{a}}(t) - v_{\mathrm{c}}(t) - E_{\mathrm{O_2}}(t) + T(t)\frac{\partial E_{\mathrm{O_2}}}{\partial T}(t)\right]. \end{aligned} \tag{A19}$$

Thus, we obtain the RC equation for the thermal terminal as:

$$i_{\mathrm{T}}(t) = \begin{pmatrix} g_{\mathrm{T,a}} & g_{\mathrm{T,c}} & g_{\mathrm{T,T}} & g_{\mathrm{T,P}} \end{pmatrix} \begin{pmatrix} v_{\mathrm{a}}(t) \\ v_{\mathrm{c}}(t) \\ T(t) \\ P(t) \end{pmatrix} - b_{\mathrm{T}}(t-h), \tag{A20}$$

where,

$$\begin{aligned} g_{\mathrm{T,a}} = \left.\frac{\partial i_{\mathrm{T}}}{\partial v_{\mathrm{a}}}\right|_{t-h} = {} & -\frac{1}{T}\left[v_{\mathrm{a}} - v_{\mathrm{c}} - E_{N_i} + T\frac{\partial E_{N_i}}{\partial T}\right]\frac{\partial i_{N_i}}{\partial v_{\mathrm{a}}} \\ & - \frac{i_{N_i}}{T}\left[1 - \frac{\partial E_{N_i}}{\partial v_{\mathrm{a}}} + T\frac{\partial}{\partial v_{\mathrm{a}}}\frac{\partial E_{N_i}}{\partial T}\right] \\ & - \frac{1}{T}\left[v_{\mathrm{a}} - v_{\mathrm{c}} - E_{\mathrm{O_2}} + T\frac{\mathrm{d}E_{\mathrm{O}}}{\mathrm{d}T}\right]\frac{\partial i_{\mathrm{O_2}}}{\partial v_{\mathrm{a}}} - \frac{i_{\mathrm{O_2}}}{T}, \end{aligned} \tag{A21}$$

$$\begin{aligned} g_{\mathrm{T,c}} = \left.\frac{\partial i_{\mathrm{T}}}{\partial v_{\mathrm{c}}}\right|_{t-h} = {} & -\frac{1}{T}\left[v_{\mathrm{a}} - v_{\mathrm{c}} - E_{N_i} + T\frac{\partial E_{N_i}}{\partial T}\right]\frac{\partial i_{N_i}}{\partial v_{\mathrm{c}}} \\ & - \frac{i_{N_i}}{T}\left[-1 - \frac{\partial E_{N_i}}{\partial v_{\mathrm{c}}} + T\frac{\partial}{\partial v_{\mathrm{c}}}\frac{\partial E_{N_i}}{\partial T}\right] \\ & - \frac{1}{T}\left[v_{\mathrm{a}} - v_{\mathrm{c}} - E_{\mathrm{O_2}} + T\frac{\mathrm{d}E_{\mathrm{O_2}}}{\mathrm{d}T}\right]\frac{\partial i_{\mathrm{O_2}}}{\partial v_{\mathrm{c}}} + \frac{i_{\mathrm{O_2}}}{T}, \end{aligned} \tag{A22}$$

$$\begin{aligned} g_{\mathrm{T,T}} = \left.\frac{\partial i_{\mathrm{T}}}{\partial T}\right|_{t-h} = {} & -\frac{c_p m}{2hT^2}[-4T(t-h) + T(t-2h)] \\ & + \left(\frac{i_{N_i}}{T^2} - \frac{1}{T}\frac{\partial i_{N_i}}{\partial T}\right)\left[v_{\mathrm{a}} - v_{\mathrm{c}} - E_{N_i} + T\frac{\partial E_{N_i}}{\partial T}\right] \\ & - i_{N_i}\frac{\partial^2 E_{N_i}}{\partial T^2} + \left(\frac{i_{\mathrm{O_2}}}{T^2} - \frac{1}{T}\frac{\partial i_{\mathrm{O_2}}}{\partial T}\right) \\ & \times \left[v_{\mathrm{a}} - v_{\mathrm{c}} - E_{\mathrm{O_2}} + T\frac{\mathrm{d}E_{\mathrm{O_2}}}{\mathrm{d}T}\right], \end{aligned} \tag{A23}$$

$$g_{\mathrm{T,P}} = \left.\frac{\partial i_{\mathrm{T}}}{\partial P}\right|_{t-h} = 0, \tag{A24}$$

$$\begin{aligned} & b_{\mathrm{T}}(t-h) = -i_{\mathrm{T}}(t-h) + \sum_k g_{\mathrm{T},k}k(t-h), \\ & k = v_{\mathrm{a}},\ v_{\mathrm{c}},\ T,\ P, \end{aligned} \tag{A25}$$

where,

$$\frac{\partial}{\partial v_{\mathrm{a}}}\frac{\partial E_{N_i}}{\partial T} = \frac{(\partial^2 E_{N_i}/(\partial x \partial T))(\partial i_{N_i}/\partial v_{\mathrm{a}})}{\partial i_{N_i}/\partial x}, \tag{A26}$$

$$\frac{\partial}{\partial v_{\mathrm{c}}}\frac{\partial E_{N_i}}{\partial T} = \frac{(\partial^2 E_{N_i}/(\partial x \partial T))(\partial i_{N_i}/\partial v_{\mathrm{c}})}{\partial i_{N_i}/\partial x} \tag{A27}$$

A.4. Pressure signal terminal

The pressure calculation follows Eqs. (17)–(19). A time-discretized form of the pressure is given as,

$$p(t) = \frac{RT(t)}{3V_g}\left[\frac{h}{F}i_{N_i}(t) + 4n_{\mathrm{H_2}}(t-h) - n_{\mathrm{H_2}}(t-2h)\right]. \tag{A28}$$

The equation for the pressure signal terminal follows,

$$i_{\mathrm{P}}(t) = \frac{P(t)}{R_{\mathrm{p}}} - p(t). \tag{A29}$$

where p denotes the pressure, while P signifies the across variable. R_{p} is the output impedance of the pressure terminal. To accurately monitor the pressure, it requires $i_{\mathrm{p}}(t) \approx 0$ and $P(t) \approx p(t)$. Thus, $R_{\mathrm{p}} = 1$. The RC equation for this terminal can be derived as,

$$i_{\mathrm{P}}(t) = \begin{pmatrix} g_{\mathrm{P,a}} & g_{\mathrm{P,c}} & g_{\mathrm{P,T}} & g_{\mathrm{P,P}} \end{pmatrix} \begin{pmatrix} v_{\mathrm{a}}(t) \\ v_{\mathrm{c}}(t) \\ T(t) \\ P(t) \end{pmatrix} - b_{\mathrm{P}}(t-h) \tag{A30}$$

where,

$$\begin{cases} g_{\mathrm{P,a}} = -\dfrac{h}{F}\dfrac{\partial i_{N_i}}{\partial v_{\mathrm{a}}}\Big|_{t-h} \\ g_{\mathrm{P,c}} = -\dfrac{h}{F}\dfrac{\partial i_{N_i}}{\partial v_{\mathrm{c}}}\Big|_{t-h} \\ g_{\mathrm{P,T}} = -\dfrac{R}{3V_g}\left[\dfrac{h}{F} i_{N_i}(t) + 4n_{N_i}(t-h) \right. \\ \quad \left. - n_{N_i}(t-2h) + T(t)\dfrac{h}{F}\dfrac{\partial i_{N_i}}{\partial T}\right]\Big|_{t-h} \\ g_{\mathrm{P,P}} = \dfrac{1}{R_{\mathrm{P}}} = 1 \end{cases} , \quad \text{(A31)}$$

$$b_{\mathrm{P}}(t-h) = -i_{\mathrm{P}}(t-h) + \sum_k g_{\mathrm{P},k} k(t-h), \quad k = v_{\mathrm{a}},\ v_{\mathrm{c}},\ T,\ P. \quad \text{(A32)}$$

Combining Eq. (A16), (A20) and (A30) yield Eq. (22).

References

[1] J.D. Dunlop, J. Giner, G. Van Ommering, J.F. Stockel, Nickel Hydrogen Cell, U.S. Patent 3867299, 1975.

[2] J.D. Dunlop, G.M. Rao, T.Y. Yi, NASA Handbook for Nickel-Hydrogen Batteries, NASA Reference Pub. 1314, September 1993.

[3] B. Wu, R.E. White, Self-discharge model of a nickel-hydrogen cell, J. Electrochem. Soc. 147 (3) (2000) 902–909.

[4] B. Wu, R.E. White, Modeling of a nickel-hydrogen cell, phase reaction in the nickel active material, J. Electrochem. Soc. 148 (6) (2001) A595–A609.

[5] H. Vaidyanathan, H. Wajsgras, G.M. Rao, Voltage and capacity stability of the hubble telescope nickel-hydrogen battery, J. Power Sources 58 (1995) 7–14.

[6] P.J. Johnson, S.W. Donley, D.C. Verrier, Orbital simulation life tests of nickel hydrogen batteries with additional non-eclipse cycles, J. Power Sources 76 (1998) 210–214.

[7] S.N. Lvov, D.D. MacDonald, Thermodynamic behavior of Ni–Cd and Ni–H_2 batteries over wide ranges of temperatures (0–200 °C), KOH concentrations (0.1–20 mol kg^{-1}) and H_2 pressure (0.1–500 bar), J. Power Sources 72 (1998) 136–145.

[8] P. Dalton, F. Cohen, International space station nickel-hydrogen battery on-orbit performance, in: Proceedings of IECEC 2002. 37th Intersociety Energy Conversion Engineering Conference, Paper #20091, 2002.

[9] P. Dalton, F. Cohen, Update on international space station nickel-hydrogen battery on-orbit performance, in: Proceedings of AIAA 2003, Paper #12066, 2003.

[10] R.A. Dougal, C.W. Brice, R.O. Pettus, G. Cokkinides, A.P.S. Meliopoulos, Virtual prototyping of PCIM systems—the virtual test bed, in: Proceedings of PCIM/HFPC '98 Conference, Santa Clara, CA, November 1998, pp. 226–234.

[11] M.R. Lightner, S.W. Director, Computer-aided design of electronic circuits, in: D.G. Fink, D. Christiansen (Eds.), Electronics Engineers' Handbook, 3rd ed., McGraw-Hill, New York, 1989, Section 27.

[12] M. Jain, A.L. Elmore, M.A. Mathews, J.W. Weidner, Thermodynamic consideration of the reversible potential for the nickel electrode, Electrochem. Acta 43 (18) (1998) 2649–2660.

[13] K.P. Ta, J. Newman, Proton intercalation hysteresis in charging and discharging nickel hydroxide electrodes, J. Electrochem. Soc. 146 (8) (1999) 2769–2779.

[14] V. Srinvasan, J.W. Weidner, J. Newman, Hysteresis during cycling of nickel hydroxide active material, J. Electrochem. Soc. 148 (9) (2001) A969–A980.

[15] D. Bernardi, E. Pawlikowski, J. Newman, A general energy balance for battery systems, J. Electrochem. Soc. 132 (1) (1985) 5–12.

[16] VTB Model Library. http://vtb.engr.sc.edu/.

[17] A.J. Juhasz, An analysis and procedure for determining space environmental sink temperatures with selected computational results, NASA/TM-2001-210063, January 2001.

[18] C.W. Gear, Numerical Initial Value Problems in Ordinary Differential Equations, Prentice-Hall, Englewood Cliffs, NJ, 1971.